Development/Plasticity/Repair

Static Magnetic Field Stimulation Enhances Shunting Inhibition via a SLC26 Family Cl⁻ Channel, Inducing Intrinsic Plasticity

Adya Saran Sinha,[1]* Sumiya Shibata,[2,3]* Yasuyuki Takamatsu,[4]* Tenpei Akita,[1,5] Atsuo Fukuda,[1] and Tatsuya Mima[6]

[1]Department of Neurophysiology, Hamamatsu University School of Medicine, Hamamatsu-shi 431-3192, Shizuoka, Japan, [2]Department of Physical Therapy, Niigata University of Health and Welfare, Niigata-shi 950-3198, Japan, [3]Institute for Human Movement and Medical Sciences, Niigata University of Health and Welfare, Niigata-shi 950-3198, Japan, [4]Department of Rehabilitation Science, Faculty of Health Sciences, Hokkaido University, Sapporo-shi 060-0812, Hokkaido, Japan, [5]Division of Health Science, Department of Basic Nursing, Hamamatsu University School of Medicine, Hamamatsu-shi 431-3192, Shizuoka, Japan, and [6]The Graduate School of Core Ethics and Frontier Sciences, Ritsumeikan University, Kyoto-shi 603-8577, Kyoto, Japan

Magnetic fields are being used for detailed anatomical and functional examination of the human brain. In addition, evidence for their efficacy in treatment of brain dysfunctions is accumulating. Transcranial static magnetic field stimulation (tSMS) is a recently developed technique for noninvasively modifying brain functions. In tSMS, a strong and small magnet when placed over the skull can temporarily suppress brain functions. Its modulatory effects persist beyond the time of stimulation. However, the neurophysiological mechanisms underlying tSMS-induced plasticity remain unclear. Here, using acute motor cortical slice preparation obtained from male C57BL/6N mice, we show that tSMS alters the intrinsic electrical properties of neurons by altering the activity of chloride (Cl⁻) channels in neurons. Exposure of mouse pyramidal neurons to a static magnetic field (SMF) at a strength similar to human tSMS temporarily decreased their excitability and induced transient neuronal swelling. The effects of SMF were blocked by DIDS and GlyH-101, but not by NPPB, consistent with the pharmacological profile of SLC26A11, a transporter protein with Cl⁻ channel activity. Whole-cell voltage-clamp recordings of the GlyH-101-sensitive Cl⁻ current component showed significant enhancement of the component at both subthreshold and depolarized membrane potentials after SMF application, resulting in shunting inhibition and reduced repetitive action potential (AP) firing at the respective potentials. Thus, this study provides the first neurophysiological evidence for the inhibitory effect of tSMS on neuronal activity and advances our mechanistic understanding of noninvasive human neuromodulation.

Key words: Cl⁻ channels; intrinsic excitability; intrinsic plasticity; shunting inhibition; SLC26A11; transcranial static magnetic field stimulation

Significance Statement

Transcranial static magnetic field stimulation (tSMS) is a recently developed noninvasive brain stimulation technique. In tSMS, a strong, small magnet placed over the skull temporarily suppresses brain functions, and its modulatory effects persist beyond the stimulation time. To elucidate the neurophysiological mechanisms of tSMS, we evaluated the excitability of mouse pyramidal neurons exposed to a static magnetic field at a strength similar to that of human tSMS using whole-cell patch-clamp experiments. We demonstrated that the static magnetic field temporarily decreased neuronal excitability by increasing the activity of a specific type of Cl⁻ channel in the plasma membrane, and it also induced transient neuronal swelling. This study reveals for the first time the neurophysiological mechanism of tSMS-induced suppression of brain functions.

Introduction

The clinical application of biomagnetism has been a powerful tool for recent breakthroughs in human neuroscience. Magnetic resonance imaging is used to visualize brain structures and cerebral metabolism. Magnetoencephalography detects brain activity in the order of milliseconds. Repetitive transcranial magnetic stimulation (rTMS) can alter human brain functions noninvasively, the mechanism of which is probably via the long-term potentiation/depression (LTP/LTD) of synaptic transmission (Hallett, 2000; Kobayashi and Pascual-Leone, 2003; Hoogendam et al., 2010; Freitas et al., 2013).

Transcranial static magnetic field stimulation (tSMS) is the latest type of biomagnetism technique (Oliviero et al., 2011; Kirimoto et al., 2014; Gonzalez-Rosa et al., 2015; Carrasco-López et al., 2017; Shibata et al., 2020, 2021). By holding a strong and compact magnet over the skull, tSMS can temporarily suppress brain function just below it and cause behavioral effects on cognition, motor control, learning, and memory (Gonzalez-Rosa et al., 2015; Nojima et al., 2019; Kirimoto et al., 2020; Tsuru et al., 2020). Furthermore, the effect of brain inhibition persists beyond the time of stimulation (Oliviero et al., 2011; Dileone et al., 2018), suggesting induction of brain plasticity in humans. As a safe, easy, and low-cost therapeutic tool, tSMS has recently been applied for neuromodulation in children (Hollis et al., 2020) and for self-administered daily treatment for neurological disorder (Di Lazzaro et al., 2021).

The neurophysiological mechanisms underlying the prolonged effects of tSMS remain to be elucidated. In contrast to rTMS, in which neuronal firing followed by synaptic transmission is repeated, tSMS does not directly produce neuronal action potentials (APs). The effects of tSMS may result from changes in the function of membrane ion channels caused by magnetic torque forces on magnetically anisotropic membrane phospholipids (Rosen, 1996; Coots et al., 2004). Thus, tSMS may induce long-lasting changes in nonsynaptic intrinsic neuronal excitability or intrinsic plasticity. Intrinsic plasticity is usually represented by the neuronal input–output (I–O) function (Zhang and Linden, 2003) and is mediated by changes in the properties of membrane ion channels (Titley et al., 2017). Moreover, intrinsic plasticity has been implicated as a cellular correlate of certain types of learning and memory (Daoudal and Debanne, 2003; Jang et al., 2020) as well as a background for some neuronal disorders, including epilepsy, Alzheimer's disease, and addiction (Beck and Yaari, 2008; Kourrich et al., 2015). However, the involvement of intrinsic plasticity in the effects of human noninvasive brain stimulation has never been hypothesized.

Here we show that tSMS induces intrinsic plasticity by increasing membrane chloride (Cl^-) conductance. This increased conductance is mediated by a specific type of Cl^- channel whose pharmacological profile is consistent with SLC26A11 (Rungta et al., 2015). Thus, this study provides the first molecular and cellular evidence for the inhibitory effects of tSMS on brain function.

Materials and Methods

Slice preparation. All procedures were in accordance with guidelines issued by the Hamamatsu University School of Medicine on the ethical use of animals for experimentation and were approved by the Committee for Animal Care and Use (2019008). All experiments were performed to minimize the number of animals used. Postnatal day (P) 21–27-old male C57BL/6N mice were anesthetized with 50–90 mg/kg intraperitoneal injection of pentobarbital and decapitated. Brains were quickly removed and placed in ice-cold oxygenated modified artificial cerebrospinal fluid (ACSF) consisting of the following (in mM): 220 sucrose, 2.5 KCl, 1.25 NaH_2PO_4, 2.0 $MgSO_4$, 0.5 $CaCl_2$, 26.0 $NaHCO_3$, and 30.0 glucose, pH 7.4. Coronal slices containing the motor cortex with a thickness of 350 µm were prepared in modified ACSF by using a vibratome (Campden Instruments). This region was identified using the mouse brain atlas (Paxinos and Franklin, 2019). Slices were allowed to recover for 60 min on nylon meshes (with 1 mm pores) placed on dishes and submerged in standard ACSF consisting of the following (in mM): 126 NaCl, 2.5 KCl, 1.25 NaH_2PO_4, 2.0 $MgSO_4$, 2.0 $CaCl_2$, 26.0 $NaHCO_3$, and 20.0 glucose, saturated with 95% O_2 and 5% CO_2 at 25–26°C.

Experimental design. To investigate the effects of a static magnetic field (SMF) on the brain, we evaluated the intrinsic excitability of mouse layer II/III pyramidal neurons in acute coronal brain slices containing the motor cortex after SMF exposure. The setup for the SMF exposure is shown in Figure 1a. The intensity of the SMF at the cortical slices was 300 mT, and the duration of exposure was 30 min. These conditions are similar to those of tSMS in humans. As in humans, effects of tSMS produce a period of ~10 min attenuated neural activity followed by waning of effects within ~11–20 min; a similar strategy to evaluate effects of SMF was devised. Coronal brain slices for the experiments were divided into three groups: control with no SMF exposure (CTRL), and following a 30 min period of SMF, groups of post-SMF 1, and post-SMF 2. AP firing induced by current injection (0.5 s) was recorded in the neurons under current-clamp conditions within 0–10 and 10–20 min after SMF exposure in the post-SMF 1 and post-SMF 2 groups, respectively (Fig. 1b). The recorded neurons were synaptically isolated by bath application of drugs that blocked both glutamatergic and GABAergic neurotransmissions, as described below.

Application of SMF (Fig. 1). Following a 1 h incubation of the slices at 25–26°C for recovery, slices on the nylon meshes were submerged in standard ACSF in thin-walled (0.5 mm) borosilicate glass beaker with the placement of a neodymium (NdFeB) magnet (10 cm × 10 cm × 3 cm) underneath. The distance between the slice tissue and the magnet surface was maintained at 1 cm. The whole slices were separated into hemispheres, and one half was positioned during incubation, such that a magnetic field of 300 mT was maintained during stimulation. This position was calibrated using a teslameter/gaussmeter (PCE Instruments). The duration of the stimulation was 30 min. The control half of the slices was not exposed to a magnetic field and was maintained at 25–26°C in standard ACSF.

Whole-cell patch-clamp recordings. The slices were then transferred to a recording chamber on the stage of an upright microscope (BX51WI; Olympus) and were continuously perfused with oxygenated ACSF at a flow rate of 2 ml/min at 25–26°C. Whole-cell patch-clamp recordings were obtained from layer II/III pyramidal neurons of the motor cortex. The electrode resistance ranged from 3 to 5 MΩ when the electrode was filled with a solution containing (in mM) 140.0 potassium methanesulfonate (CH_3SO_3K), 10.0 KCl, 2.0 $MgCl_2$, 10.0 HEPES, 3.0 Na_2 ATP, 0.2 Na GTP, 1.0 EGTA, pH adjusted to 7.3 with KOH, and an osmolarity value of 310 mOsm. The liquid junction potential (LJP) was calculated to be 4.8 mV and corrected during the recording. In another set of experiments, a high Cl^- internal solution of the following composition (in mM) was used: 150.0 KCl, 2.0 $MgCl_2$, 10.0 HEPES, 3.0 Na_2 ATP, 0.2 Na GTP, 1.0 EGTA, with pH adjusted to 7.3 with KOH, and osmolarity of 306 mOsm. The corresponding calculated LJP value of 6.8 mV was corrected during the recording. Voltage changes were recorded using a MultiClamp 700B amplifier (Axon Instruments) with a Bessel prefilter at 5 kHz, and digitized at 25 kHz using a Digidata 1440A data acquisition system (Axon Instruments). Recordings were performed in the presence of bath-applied ionotropic glutamate receptor blockers: 10 µM 6-cyano-7-nitroquinoxaline-2,3-dione (CNQX), 50 µM D-2-amino-5-phosphonopentanoic acid (D-AP5), and 50 µM picrotoxin (PTX), a GABA$_A$ receptor antagonist. Additionally, during rescue experiments, either 300 µM 4,4'-diisothiocyano-2,2'-stilbenedisulfonic acid (DIDS) or 200 µM
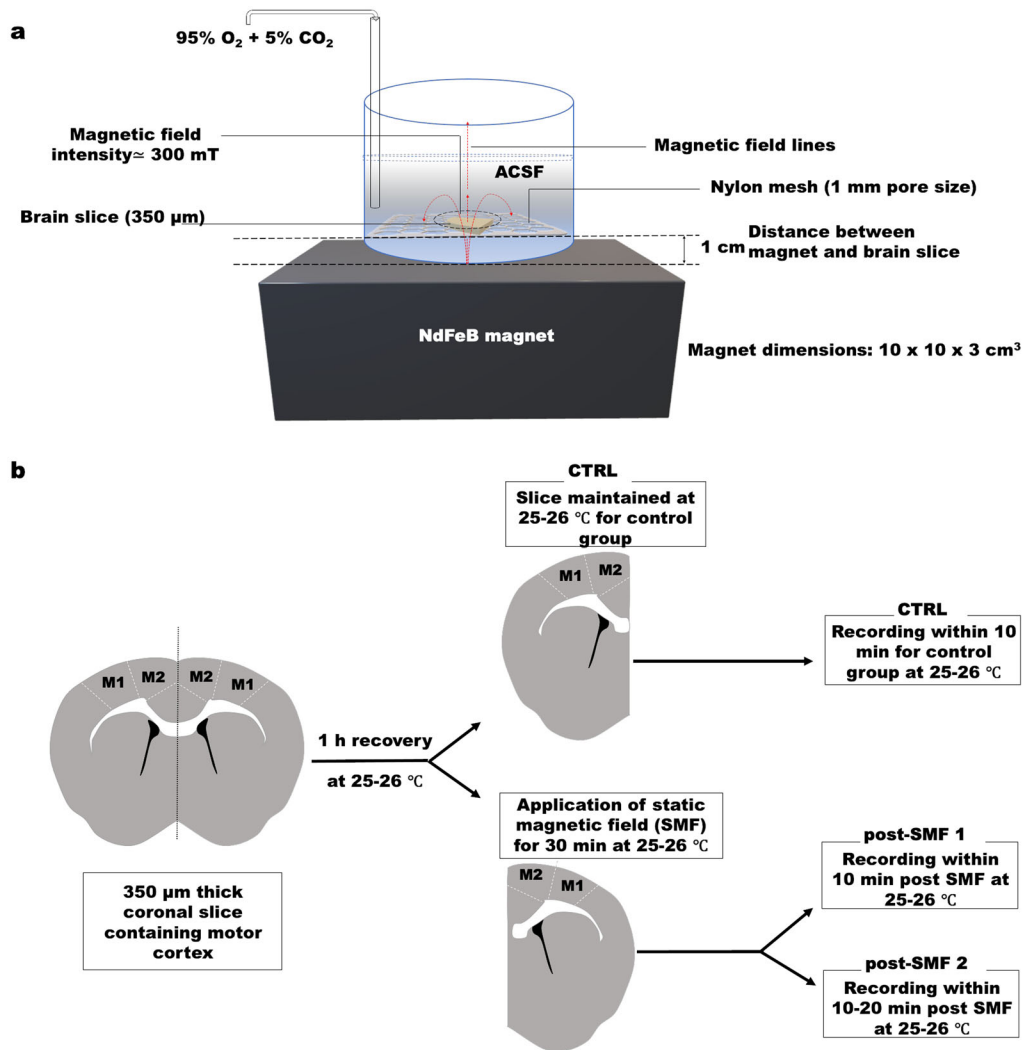
Figure 1. Application of SMF and strategy for our experiments. *a*, Setup for SMF exposure using a NdFeB magnet. The ex vivo motor cortical slices were placed on a nylon mesh with a pore diameter of 1 mm and submerged in ACSF continuously bubbled with an oxygen and carbon dioxide mixture (95% O_2 + 5% CO_2) at 25–26℃. The distance between the surface of the slice and the magnet was maintained at 1 cm. *b*, Workflow for experiments. After recovery for 1 h at 25–26℃, the two hemispheres of the coronal brain slices were separated and assigned to three groups: control without SMF exposure (CTRL), post-SMF 1, and post-SMF 2. Current-clamp recordings were performed from layer II/III pyramidal neurons—0–10 min or 11–20 min after 30 min of SMF exposure in the post-SMF 1 and post-SMF 2 groups, respectively.

5-nitro-2-(3-phenylpropylamino)benzoic acid (NPPB) was applied in the bath. Furthermore, for additional experiments, a more specific blocker for SLC26A11-mediated currents, *N*-2-naphthalenyl-2-[(3,5-dibromo-2,4-dihydroxyphenyl) methylene] glycine hydrazide (GlyH-101), at 50 μM concentration was bath applied.

To understand the current–voltage (I–V) characteristics of the enhanced Cl^- currents, we performed voltage-clamp recordings for GlyH-101-sensitive currents. We used the internal solution and drug cocktail combination together with the voltage step protocol reported earlier (Rungta et al., 2015) for isolation of SLC26A11-mediated currents. The internal solution of the following composition (in mM) was used: 108.0 CsCl, 8.0 TEA-Cl, 8.0 K-gluconate 2.0 $MgCl_2$, 10.0 HEPES, 4.0 Na_2 ATP, 0.2 Na GTP, 1.0 EGTA, with pH adjusted to 7.3 with CsOH, and osmolarity of 290 mOsm. The corresponding calculated LJP value of 4.8 mV was corrected during the recording. The bath solution during this experiment contained 10 μM CNQX, 50 μM PTX, 50 μM D-AP5, 50 μM nickel, 60 μM cadmium, and 100 μM 4-aminopyridine. GlyH-101-sensitive currents were obtained by subtracting the current response obtained by the voltage step protocol in the presence of 50 μM GlyH-101 from the current response obtained without GlyH-101.

Electrophysiological analysis. The pClamp suite was used, including Clampex 10.7 software for data acquisition and Clampfit 10.4 for analysis. Records obtained with series resistance <25 MΩ were selected for analysis. To evaluate the input resistance (R_{In}) of the recorded neurons, hyperpolarizing currents with amplitudes starting at −60 pA and decreasing by 20 pA were repeatedly injected for 500 ms. The voltage responses obtained were plotted against the corresponding current injection amplitudes to create a current–voltage relationship. The data points were then fitted using linear regression analysis. The calculated slope indicates the R_{In} of the recorded neuron. The rheobase current, that is, the amount of current injection at which a neuron fires one AP, was estimated by applying depolarizing current steps of 500 ms in 20 pA step increments. The repetitive AP firings elicited by the depolarizing current steps were used to examine the I–O curve of the recorded neurons. Furthermore, short (2 ms) depolarizing pulses were applied to induce single APs, and waveform parameters of AP amplitude, half-width, maximum rise, and decay slope were analyzed. The resting membrane potential (RMP) was calculated from the trace of the zero current injection level before application of the short-pulse protocol. The AP amplitude was calculated from RMP to AP peak voltage. The AP threshold voltage was determined at the inflection point where the AP was triggered.

Chemicals. PTX was from Tocris Bioscience. D-AP5, NPPB, and GlyH-101 were from Cayman Chemical. DIDS and TTX were from Wako, Fujifilm. CNQX and 4-AP were from Sigma-Aldrich.

Neuronal size analysis. Surface area and perimeter analyses were performed using Fiji (ImageJ) platform, version 2.1.0/1.53 C. Briefly, IR-DIC 8 bit images were obtained during electrophysiological recordings under a 40× objective. From the images, neurons with a well-defined pyramidal-shaped soma and sharp contrasts along the edges were selected for analysis. The freehand selection tool was used to define the region of interest (ROI). These ROIs were further refined using the selection brush tool with a 2 pixels tip. Then, using the measurement dialog box, parameters of surface area and perimeter were analyzed for the selected ROIs. Measurements from cells within a single slice were averaged to obtain a single data point. Therefore, the number of data points in plot indicates the number of slices analyzed.

Statistical analysis. Statistical analysis of data obtained by patch-clamp experiments was performed using IBM SPSS Ver.23 software. In brief, the data were tested for normality and equality of variance using the Kolmogorov–Smirnov (K–S) test and Levene's test, respectively. For independent samples, two-sided t test with confidence interval set at 95% was used for comparisons between the two groups. For multiple group comparisons, one-way ANOVA was performed, followed by a post hoc Ryan–Einot–Gabriel–Welsch F test. However, if the K–S statistic confirmed a non-normal distribution, the one-sided Mann–Whitney U test was employed for the two groups, and for multiple groups, the K–W test followed by stepwise step-down comparisons was used. Data are presented as mean ± standard error of the mean (SEM). Statistical analysis of the imaging data was also performed based on a similar algorithm. Statistical significance is presented as follows: $*p < 0.05$, $**p < 0.01$, $***p < 0.001$, ns (not significant).

Results

Temporary suppression of neuronal excitability after SMF exposure

The relationship of injected currents to the number of AP spikes (I–O curve) showed that their numbers in the post-SMF 1 group were significantly lower than those in the CTRL and post-SMF 2 groups over the full range of injected currents [Fig. 2a,b; Kruskal–Wallis test (K–W test); $**p < 0.01$]. Rheobase, the minimum current necessary for AP generation, was significantly higher in the post-SMF 1 group (313.75 ± 26.82 pA; $n = 16$ cells, five mice) than that in the CTRL group (183 ± 17.49 pA; $n = 20$ cells, five mice; $p = 0.000136$; Fig. 2c). The rheobase in the post-SMF 2 group (197.14 ± 19.87 pA; $n = 21$ cells, six mice) was similar to that in the CTRL group. The higher rheobase suggested changes in the passive membrane properties in the post-SMF 1 group. Indeed, the R_{In}, the reciprocal of membrane ion conductance under resting conditions, in the post-SMF 1 group (69.35 ± 6.34 MΩ; $p = 0.003$) was significantly lower than that in the CTRL (128.1 ± 16.51 MΩ) and post-SMF 2 groups (119.75 ± 13.12 MΩ), whereas the R_{In} in the CTRL and post-SMF 2 groups was statistically similar (Fig. 2d). Together, these findings indicate that 30 min of exposure to SMF temporarily suppressed the excitability of pyramidal neurons by reducing R_{In}, that is, by increasing the resting membrane conductance, and the excitability recovered within 20 min after the end of the exposure.

The increase in the resting membrane conductance can be mediated by various ions. The RMP shifts toward a more negative or positive value on an increase in the K$^+$ or Na$^+$ conductance, according to the polarity of the equilibrium potential for K$^+$ or Na$^+$, respectively. However, the RMP did not differ between the three groups (CTRL, -70.65 ± 1.80 mV; post-SMF 1, -70.13 ± 1.89 mV; and post-SMF 2, -70.91 ± 1.73 mV; $p = 0.931$; Fig. 3a), suggesting that the increase in K$^+$ or Na$^+$ conductance was less likely. The higher rheobase may also have resulted from an increase in the threshold membrane voltage level for AP generation; however, it also did not differ between

them (Fig. 4a). Moreover, the parameters characterizing the waveform of a single AP remained unchanged (Figs. 3b, 4b–e). Thus, the voltage-gated Na$^+$ and K$^+$ channels responsible for AP generation appeared to be unaffected by the SMF exposure. A previous study (Rosen, 2003a) reported a reduction in Na$^+$ conductance in the GH3 cell line within 200 s after the end of the SMF exposure. In our experimental setup, it took ∼4–8 min to complete the AP recordings after the SMF exposure. Thus, the reduced Na$^+$ conductance, if any, was restored to its initial level by the time of data acquisition in our experiments. Therefore, the increased resting membrane conductance underlying the temporary suppression of neuronal excitability within 10 min of SMF exposure was likely mediated by ions other than Na$^+$ and K$^+$.

SMF exposure increases resting membrane conductance through Cl$^-$ channels

The equilibrium potential for Cl$^-$ under the experimental conditions described above was approximately -60 mV. Thus, the increase in Cl$^-$ conductance, if any, would have had little impact on the RMP. Therefore, to test whether the SMF increased Cl$^-$ conductance, we next examined passive membrane properties and AP firing using a patch pipette solution containing a high concentration of Cl$^-$ (154 mM) and compared them between the conditions of the CTRL and post-SMF 1 group. If the SMF increased the Cl$^-$ conductance under this condition, it would shift the RMP toward a more positive value, because the equilibrium potential for Cl$^-$ was high (∼0 mV). Indeed, we found a significant depolarization of the RMP in the post-SMF 1 group (-70.15 ± 1.05 mV; $n = 18$ cells, five mice; $p = 0.016$) in comparison with the CTRL group (-73.69 ± 1.33 mV; $n = 18$ cells, five mice; Fig. 5a). Higher rheobase (Fig. 5b), lower R_{In} (Fig. 5c), and a smaller number of AP spikes (Fig. 5d) were also reproduced under this condition. The parameters of the AP waveform were unchanged (Figs. 5e, 6), except for a small but significant reduction in the AP amplitude after SMF exposure (CTRL, 109.31 ± 1.64 mV; post-SMF 1, 102.37 ± 1.56 mV; $p = 0.004$; Fig. 6b). Thus, the SMF exposure temporarily suppressed neuronal excitability by enhancing resting Cl$^-$ conductance.

The ligand-gated Cl$^-$ channel γ-aminobutyric acid receptors (GABA$_A$R) are important regulators of neuronal excitability. However, the effect of SMF on intrinsic excitability was independent of GABAergic action, as the experimental conditions included PTX, a potent blocker of these channels. Identification of the other types of Cl$^-$ channels involved in SMF action is inherently complex because of the lack of highly specific and sensitive pharmacological tools at our disposal (Verkman and Galietta, 2009). However, a reasonable assessment of the type of Cl$^-$ channel responsible for the SMF action can be obtained from their sensitivity to classical Cl$^-$ channel blockers with divergent spectra. Therefore, we examined the effects of these drugs on the shifts in RMP, R_{In}, and rheobase after SMF exposure using a high Cl$^-$ pipette solution. Blockers were applied during the SMF exposure. We found that a nonselective blocker, DIDS (300 μM), significantly inhibited the SMF-induced shifts of all parameters (Fig. 7a–c; post-SMF 1 + DIDS), whereas another nonselective blocker, 5-nitro-2-(3-phenylpropylamino) benzoic acid (NPPB; 200 μM), had no effect (Fig. 5a–c; post-SMF 1 + NPPB).

In addition, since increase in Cl$^-$ conductance is often associated with increase in cell volume (Akita and Okada, 2014), we compared the perimeter and surface area of neuronal somata before whole-cell recording between the CTRL and post-SMF 1 groups (Fig. 8a,b). We found that both perimeter (CTRL, 45.04
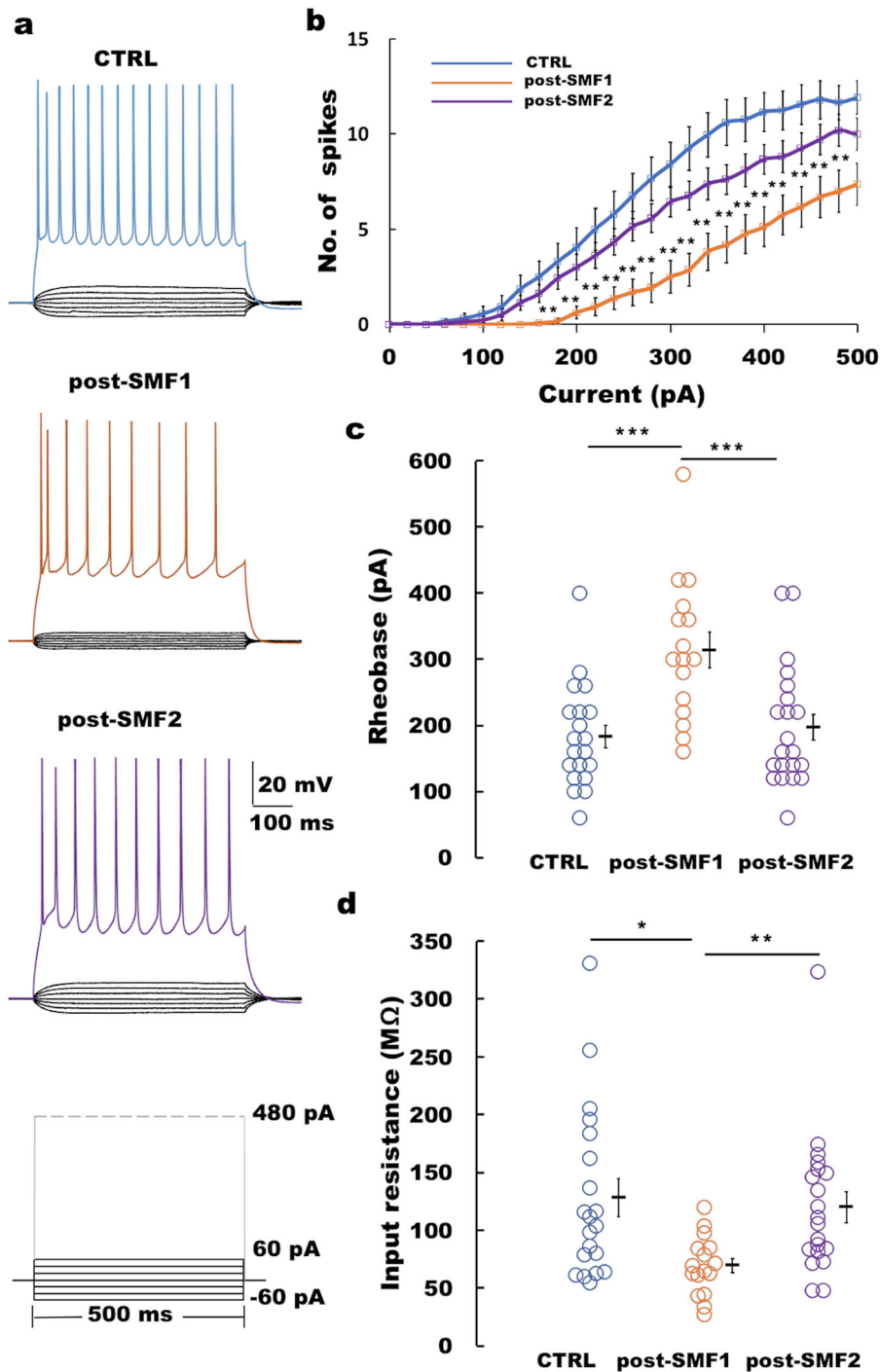
Figure 2. Reduced intrinsic excitability of layer II/III pyramidal neurons of the motor cortex following SMF application. ***a***, Representative subthreshold current injections (from −60 to +60 pA) with consequent voltage responses and repetitive firing by suprathreshold current injection (+480 pA) in the control (CTRL; blue), post-SMF 1 (orange), and post-SMF 2 (purple) groups. At the same subthreshold current injection, the voltage responses decreased in the post-SMF 1 group. At +480 pA current injection, the number of spikes decreased in the same group. ***b***, A significant decrease (K−W test; **$p < 0.01$) in the I–O relationship for the post-SMF 1 (orange) group in comparison with both CTRL (blue) and post-SMF 2 (purple) groups. Error bars represent SEM. ***c***, ***d***, Individual data points are shown as open circles in blue (CTRL, $n = 20$), orange (post-SMF 1, $n = 16$), and purple (post-SMF 2, $n = 21$). The mean values are indicated by solid bars next to the data points. Error bars represent SEM. Rheobase from layer II/III pyramidal neurons significantly increased in the post-SMF 1 group compared with CTRL and post-SMF 2 (one-way ANOVA; $p = 0.000136$; post hoc, Ryan−Einot−Gabriel−Welsch F test; post-SMF 1 vs post-SMF 2 with **$p < 0.01$; post-SMF 1 vs CTRL with *$p < 0.05$) groups (***c***). Input resistance of pyramidal neurons significantly decreased in the post-SMF 1 group (K−W test; **$p < 0.01$; post hoc, stepwise step-down; post-SMF 1 vs post-SMF 2 with **$p < 0.01$; post-SMF 1 vs CTRL with *$p < 0.05$; ***d***).

± 1.27 µm, $n = 17$ slices, 6 cells/slice; post-SMF 1, 53.80 ± 0.57 µm, $n = 17$ slices, 5.5 cells/slice, 8 mice, $p = 1.0 \times 10^{-5}$; Fig. 8d) and surface area (CTRL, 121.41 ± 6.13 µm^2; post-SMF 1, 167.62 ± 3.60 µm^2; $p = 3.0 \times 10^{-6}$; Fig. 8e) were significantly larger in the post-SMF 1 group. DIDS treatment blocked this

transient increase in perimeter (CTRL, 45.04 ± 1.27 µm; post-SMF 1 + DIDS, 46.05 ± 0.59 µm; $n = 13$ slices, 6 cells/slice, 5 mice) and surface area of neuronal somata (CTRL, 121.41 ± 6.13 µm^2; post-SMF 1 + DIDS, 128.50 ± 3.03 µm^2; Fig. 8c–e). Thus, the conductance through a DIDS-sensitive, NPPB-insensitive type of

Cl⁻ channel would have been predominantly increased by SMF, thereby temporarily suppressing the excitability of pyramidal neurons and also causing neuronal swelling.

Among neuronal Cl⁻ channels, the one with a pharmacological profile consistent with our findings of DIDS sensitivity and NPPB insensitivity was the channel function of the transporter protein SLC26A11 reported by Rungta et al. (2015). In that report, they showed that CFTR inhibitor GlyH-101 inhibited

Cl⁻ transport via SLC26A11 by 80% at 10 µM concentration. Therefore, we investigated whether GlyH-101 could rescue the depression of intrinsic excitability of neurons after SMF using the high Cl⁻ (154 mM) internal solution. The comparisons of I–O curves revealed a reversal of effect of SMF following GlyH-101 application. Moreover, the number of AP spikes fired by these neurons exceeded those of CTRL neurons significantly (Fig. 9a,b; K–W test; ***$p < 0.001$). We also observed a reversal of rheobase currents (Fig. 9c), R_{In} (Fig. 9d), and RMP levels (Fig. 9e) similar to CTRL group, respectively. Thus, the Cl⁻ channel affected by SMF application was sensitive to DIDS and GlyH-101 but not to NPPB, suggesting the SLC26A11 channel.

SMF increases voltage-dependent GlyH-101-sensitive currents both at subthreshold and depolarized membrane potentials
Rungta et al. (2015) reported that the Cl⁻ currents mediated by SLC26A11 in layer 4 cortical neurons were dependent on the membrane voltage. We therefore next evaluated if Cl⁻ currents modulated by SMF exhibit any voltage dependence. Using the same internal solution, blockers and voltage step protocol (from −70 to +20 mV, 300 ms duration) as in Rungta et al. (2015), whole-cell Cl⁻ currents were recorded before and after application of 50 µM GlyH-101, and the GlyH-101-sensitive current component was isolated by subtraction and compared between the CTRL and post-SMF 1 groups (Fig. 10a). The peak current–voltage (I–V) plots (Fig. 10b) revealed that the GlyH-101-sensitive current component was significantly
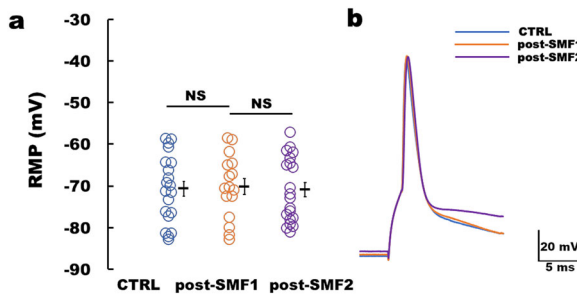

Figure 3. RMP values and single AP waveform following SMF application. *a*, Individual data points are shown as open circles in blue (CTRL, n = 20), orange (post-SMF 1, n = 16), and purple (post-SMF 2, n = 21). The mean values are indicated by solid bars next to the data points. Error bars represent SEM. The RMP values were not significantly different among the three groups (one-way ANOVA; ns). *b*, Representative single AP waveforms elicited by a short-pulse (2 ms) protocol in the CTRL (blue), post-SMF 1 (orange), and post-SMF 2 (purple) groups. SMF application had no apparent effect on the AP waveform.
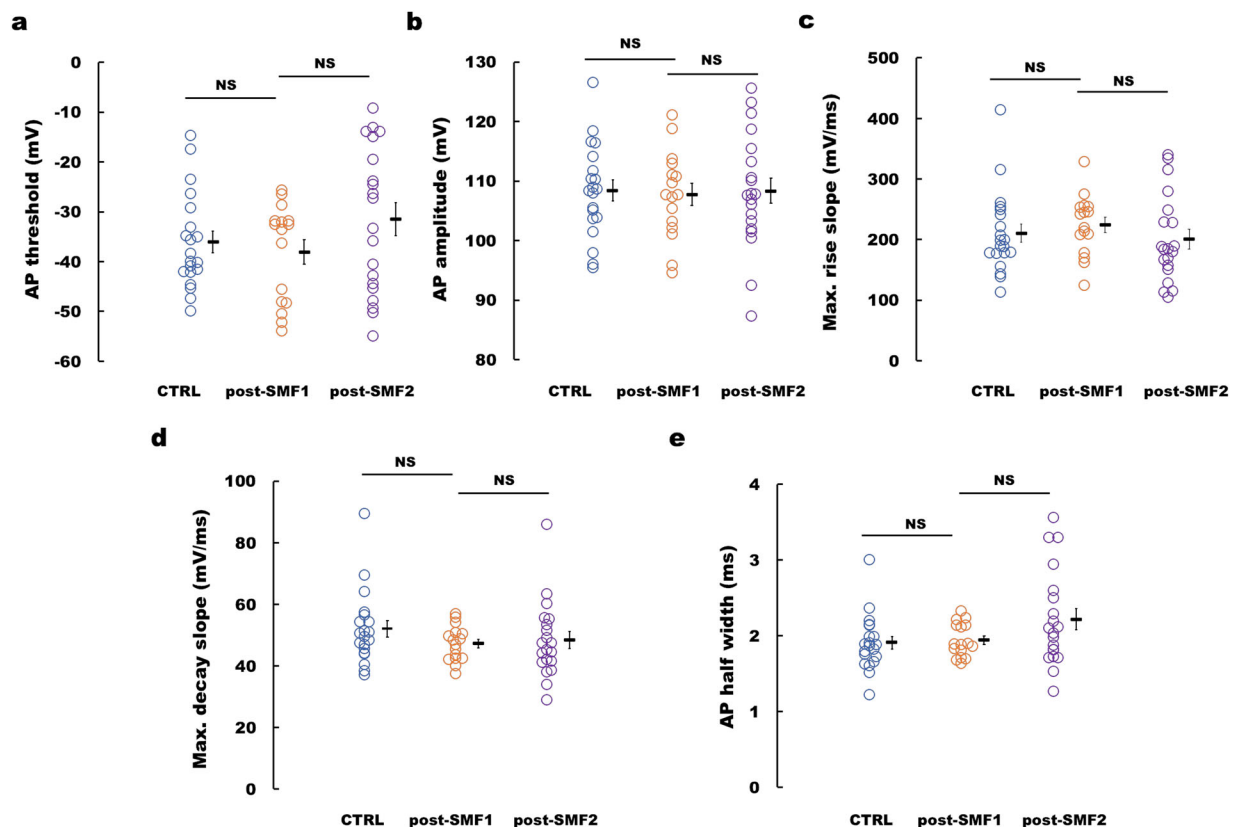

Figure 4. AP parameters following SMF application. *a–e*, Individual data points are shown as open circles in blue (CTRL, n = 20), orange (post-SMF 1, n = 16), and purple (post-SMF 2, n = 21). The mean values are indicated by solid bars next to the data points. Error bars represent SEM. AP thresholds (CTRL, −36.08 ± 2.16 mV; post-SMF 1, −38.09 ± 2.46 mV; and post-SMF 2, −31.48 ± 3.30 mV; p = 0.400; *a*), AP amplitudes (CTRL, 108.45 ± 1.75 mV; post-SMF 1, 107.77 ± 1.84 mV; and post-SMF 2, 108.38 ± 2.11 mV; p = 0.946; *b*), maximum rise slopes (CTRL, 210.50 ± 15.20 mV/ms; post-SMF 1, 224.26 ± 12.49 mV/ms; and post-SMF 2, 200.78 ± 16.09 mV/ms; p = 0.286; *c*), maximum decay slopes (CTRL, 52.09 ± 2.66 mV/ms; post-SMF 1, 47.26 ± 1.41 mV/ms; and post-SMF 2, 48.41 ± 2.75 mV/ms; p = 0.394; *d*), and AP half-maximal widths (CTRL, 1.91 ± 0.08 ms; post-SMF 1, 1.94 ± 0.06 ms; and post-SMF 2, 2.22 ± 0.14 ms; p = 0.08; *e*) were not significantly different among the three groups (one-way ANOVA, ns).
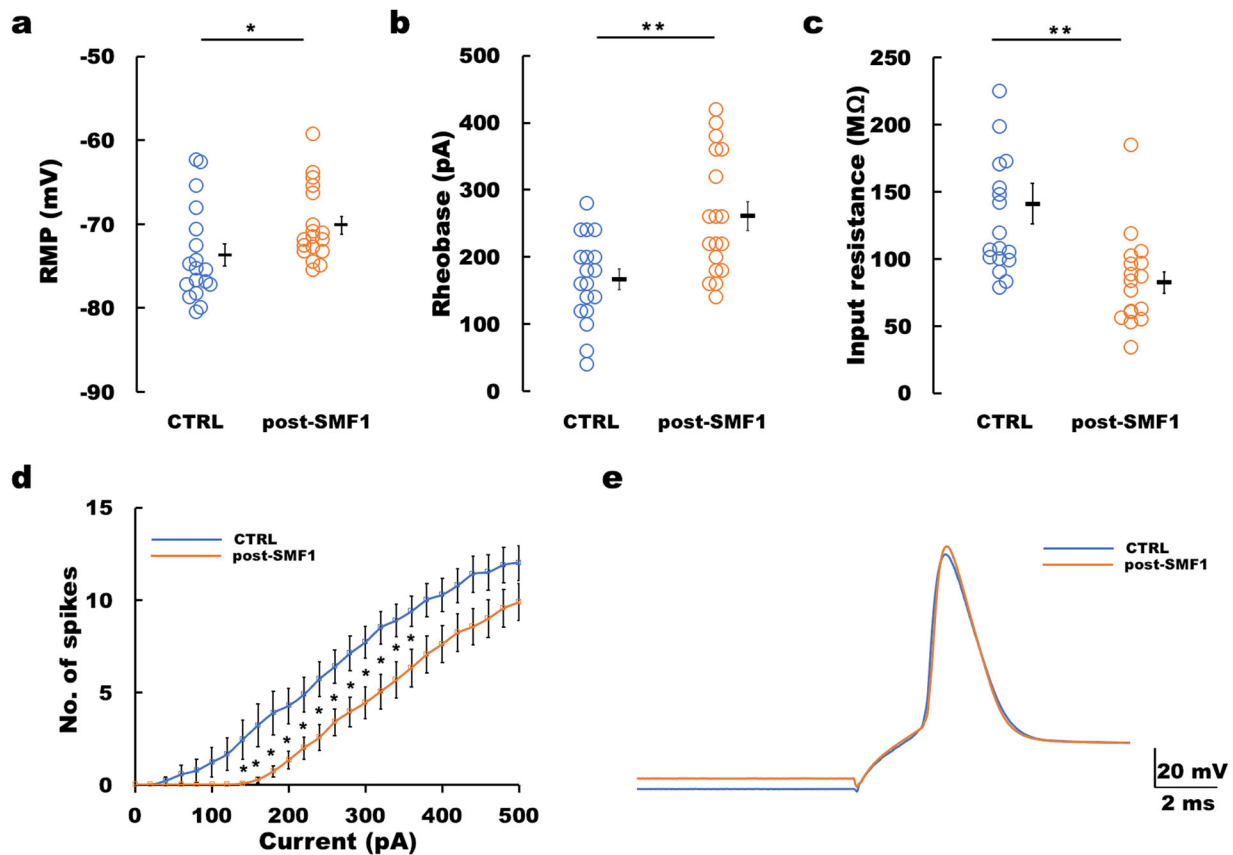
Figure 5. Intrinsic excitability of layer II/III pyramidal neurons of the motor cortex under high $[Cl^-]_i$ internal solution. ***a–c***, Individual data points are shown as open circles in blue (CTRL, $n = 18$) and orange (post-SMF 1, $n = 18$). The mean values are indicated by solid bars next to the data points. Error bars represent SEM. ***a***, Quantitative analysis of current-clamp recordings using 154 mM Cl^- internal solution revealed a significantly depolarized RMP in the post-SMF 1 group (Mann–Whitney U test; *$p < 0.05$), indicating an enhancement of resting Cl^- conductance (compare Fig. 3*a*). ***b***, Rheobase was significantly increased in the post-SMF 1 group (t test; **$p < 0.01$). ***c***, Input resistance of neurons from the post-SMF 1 group was significantly reduced (t test; **$p < 0.01$). ***d***, A significant decrement in the input–output relationship for the post-SMF 1 group (orange) in comparison with the CTRL group (blue; Mann–Whitney U test; *$p < 0.05$). Error bars represent SEM. ***e***, Representative single AP waveforms elicited by a short-pulse (2 ms) protocol in the CTRL (blue) and post-SMF 1 (orange) groups.

enhanced after SMF application in the whole voltage range from −70 to +20 mV (at −70 mV, post-SMF 1: 32.24 ± 7.20 pA, $n = 14$ cells, four mice; CTRL: 4.27 ± 7.55 pA, $n = 14$ cells, five mice, $p = 0.012548$; at −60 mV, post-SMF 1: 48.96 ± 8.26 pA, $n = 14$ cells, four mice; CTRL: 12.56 ± 6.35 pA, $n = 14$ cells, five mice, $p = 0.001727$ and at +20 mV, post-SMF 1: 627.57 ± 72.59 pA, $n = 14$ cells, four mice; CTRL: 233.61 ± 43.19 pA, $n = 14$ cells, five mice, $p = 0.000082$). The component further consisted of the rapidly activating and inactivating current component generated at the beginning of the voltage step and the slowly activating current component throughout the voltage step. The rapid component was already generated at the subthreshold levels of the voltage steps. The slow component showed outward rectification with increasing voltage, similar to the current reported by Rungta et al. (2015). Both the rapid and slow current components were significantly enhanced after SMF application. Thus, the rapid Cl^- current component induced by SMF is responsible for the shunting inhibition that offsets membrane excitability at subthreshold voltages and the slow Cl^- current component is responsible for the reduction of AP spikes during repetitive AP firing at depolarized voltages.

TTX-sensitive Na^+ currents contribute to induction of SMF action
Considering that Cl^- entry is secondarily driven by the electrochemical driving force for Na^+, we investigated the role of

tetrodotoxin (TTX)-sensitive Na^+ channel activity in the SMF-induced effects. For this purpose, we applied 1 µM TTX during 30 min of SMF application and evaluated RMP, R_{In} and rheobase currents after TTX washout using the high Cl^- pipette solution. We found that the TTX treatment abolished the effects of SMF. RMP (CTRL: −73.69 ± 1.33 mV, $n = 18$ cells, five mice; post-SMF1 + TTX: −74.20 ± 1.71 mV, $n = 15$ cells, four mice) remained similar to the CTRL group, indicating that the increase in basal conductance after SMF was prevented. Similarly, the changes in R_{In} and rheobase currents became nonsignificant (data not shown). Thus, the Na^+ entry through voltage-gated Na^+ channels was found to be necessary for the SMF-induced increase in membrane Cl^- conductance.

Discussion
Our electrophysiological experiments investigating the mechanisms underlying tSMS action show that mouse pyramidal cells exhibited same prolonged suppression of intrinsic excitability (∼10 min) after exposure to the similar magnetic parameters as in human tSMS studies (Oliviero et al., 2011). This intrinsic plasticity is mediated by a Cl^- channel sensitive to both DIDS and GlyH-101. The I–V characteristics of these GlyH-101-sensitive Cl^- currents indicate SMF action produces increase in conductance at both subthreshold and depolarized membrane potentials essentially enhancing a shunting inhibition.
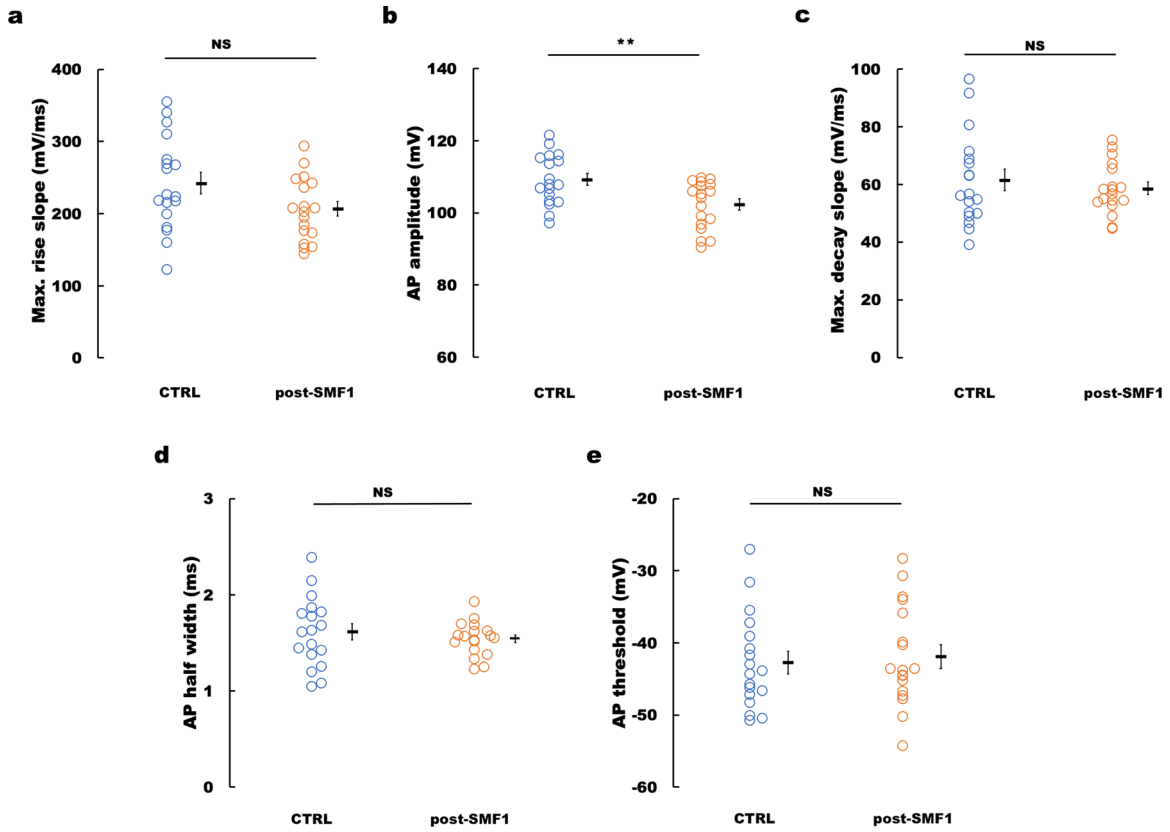
Figure 6. AP parameters under high $[Cl^-]_i$ internal solution following SMF application. The maximum rise slopes (**a**), maximum decay slopes (**c**), AP half-maximal widths (**d**), and AP threshold voltages (**e**) were not significantly different between the CTRL and post-SMF 1 groups (*t* test; ns). **b**, AP amplitudes were significantly reduced in the post-SMF 1 group (*t* test; **$p < 0.01$).
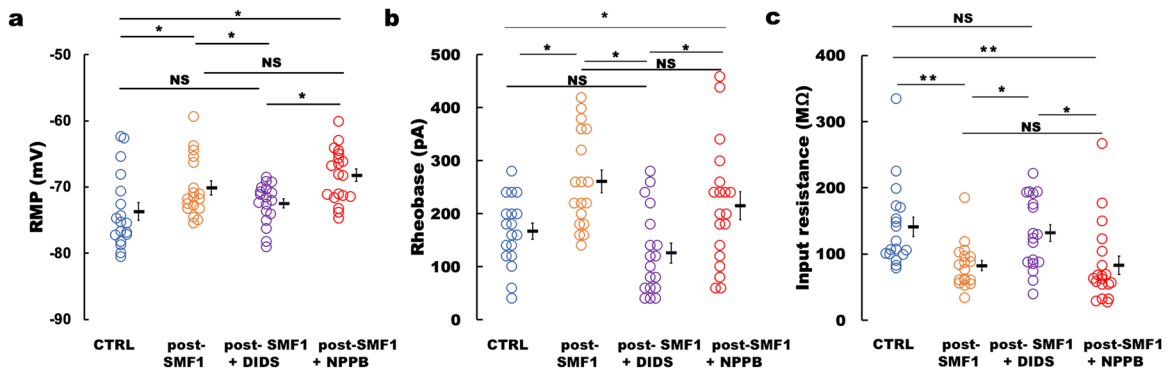

Figure 7. Inhibition of SMF-induced shifts in RMP, rheobase, and input resistance by DIDS, not by NPPB. **a–c**, Individual data points are shown as open circles in blue (CTRL, $n = 18$), orange (post-SMF 1, $n = 18$), purple (post-SMF 1 + DIDS, $n = 18$), and red (post-SMF 1 + NPPB, $n = 18$). The mean values are indicated by solid bars next to the data points. Error bars represent SEM. **a**, The significant increase in RMP after SMF application was reversed by DIDS (300 µM) treatment; however, not by NPPB (200 µM) application ($p = 0.003$; CTRL vs post-SMF 1 + DIDS, ns; CTRL vs post-SMF 1, **$p < 0.01$; post-SMF 1 vs post-SMF 1+ NPPB, ns). **b**, The significant increase in rheobase levels was also reversed following DIDS treatment. NPPB treatment showed no effect ($p = 0.000149$; CTRL vs post-SMF 1+ DIDS, ns; CTRL vs post-SMF 1, *$p < 0.05$; post-SMF 1 + DIDS vs post-SMF 1, *$p < 0.05$; post-SMF 1 vs post-SMF 1 + NPPB, ns). **c**, Application of DIDS rescued the reduction in input resistance after SMF application. However, NPPB treatment showed no effect (**$p < 0.01$; CTRL vs post-SMF 1 + DIDS, ns; CTRL vs post-SMF 1, **$p < 0.01$; post-SMF 1 + DIDS vs post-SMF 1, **$p < 0.01$; post-SMF 1 vs post-SMF 1 + NPPB, ns).

The neuronal membrane expresses different classes of Cl^- channels and transport proteins (Duran et al., 2010). In tandem, they regulate pH, cell volume, and GABAergic and glycinergic neurotransmission, enabling a multitude of physiological functions related to neuronal migration, brain development, and information processing. The identity of the Cl^- channels involved in the SMF action may be surmised based on their pharmacological sensitivities to two broad-spectrum Cl^- channel

blockers, DIDS, and NPPB. Among the voltage-gated Cl^- channels (ClC family), ClC-2 channels are expressed in neurons and other cell types, including astrocytes, and are active at voltages close to the RMP (Jentsch and Pusch, 2018). As a candidate mediator of the SMF action, ClC-2 channels are feasible; however, their pharmacological profiles indicate poor antagonism by DIDS (Alexander et al., 2013). In addition, they are sensitive to the NPPB blocks. This spectrum is in contrast to our
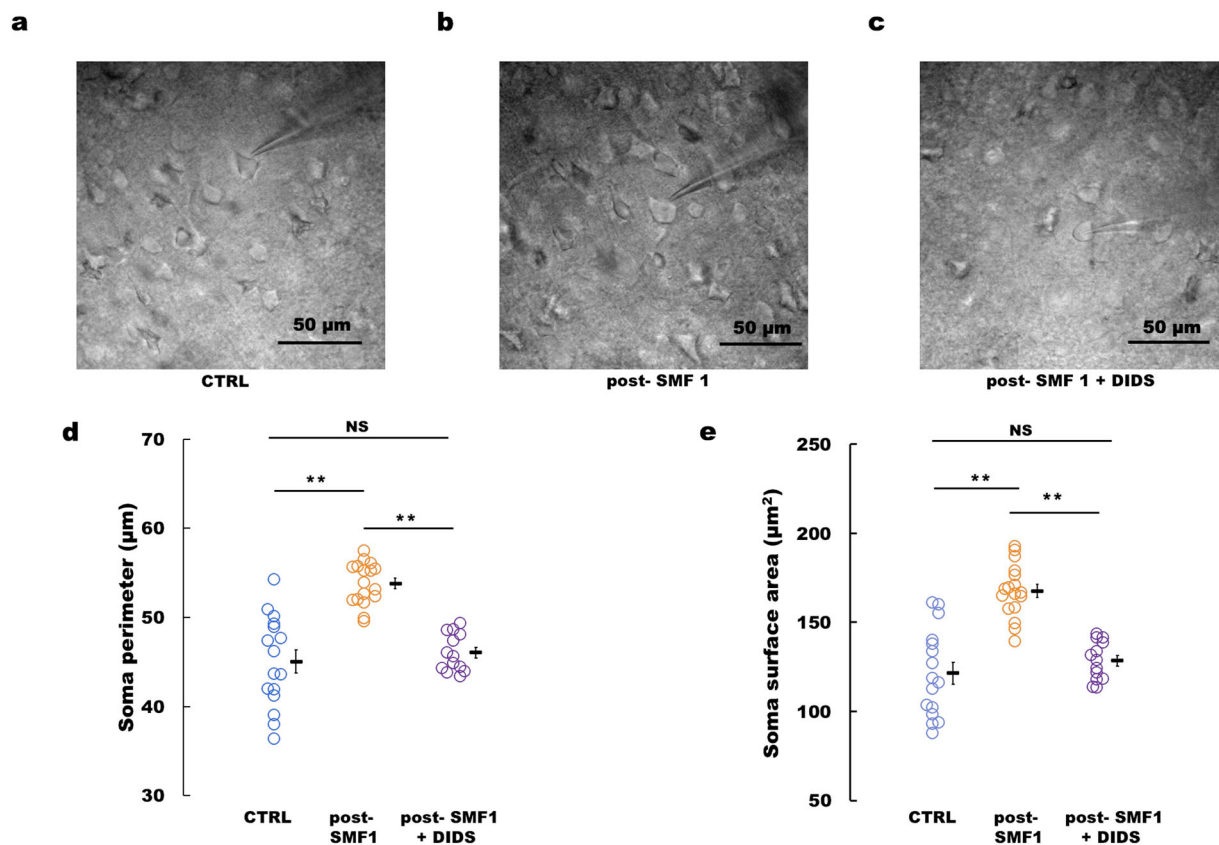
Figure 8. Transient neuronal swelling following SMF application. Examples of IR-DIC images from the motor cortical slices incubated with CTRL (***a***), post-SMF 1 (***b***), and post-SMF 1 + DIDS (300 µM; ***c***). Pyramidal neurons in the post-SMF 1 slice had an apparent swollen appearance unlike in the DIDS-incubated slices. Scale bar, 50 µm. ***d***, Pyramidal neurons from slices in the post-SMF 1 group (orange open circles, $n = 17$ slices, 8 mice) significantly increased in the soma perimeter when compared with that in the CTRL group (blue open circles, $n = 17$ slices, 8 mice). DIDS treatment (purple open circles, $n = 13$ slices, 6 mice) prevented this transient increase in the soma perimeter (**$p < 0.01$; CTRL vs post-SMF 1 + DIDS, ns; CTRL vs post-SMF 1, **$p < 0.01$; post-SMF 1 + DIDS vs post-SMF 1, **$p < 0.01$). ***e***, Quantitative analysis of the soma surface area of neurons showed a significant increase in the post-SMF 1 group when compared with both CTRL and DIDS application groups (*$p < 0.01$; CTRL vs post-SMF 1 + DIDS, ns; CTRL vs post-SMF 1, **$p < 0.01$; post-SMF 1 + DIDS vs post-SMF 1, **$p < 0.01$).

experimental findings. Another prospective target is volume-sensitive outwardly rectifying (VSOR) anion channels (Akita and Okada, 2014) important in cell volume regulation. These VSOR channels are reportedly sensitive to both DIDS and NPPB (Inoue et al., 2005). Our pharmacological profiling experiments indicated that the SMF-activated Cl^- conductance was insensitive to NPPB action, thereby deviating from classical VSOR channel properties.

Among the other mediators of neuronal Cl^- transport, a favorable pharmacological profile consistent with our findings of DIDS and GlyH-101 sensitivity and NPPB insensitivity is the channel activity of the transporter protein SLC26A11 (Rungta et al., 2015, Rahmati et al., 2016). These proteins are reported to express at moderate to high levels in the neocortex (Rahmati et al., 2013) and accumulate Cl^- intracellularly accompanying sustained increase in $[Na^+]_i$ during cytotoxic neuronal swelling (Rungta et al., 2015). In addition to the increase in Cl^- conductance, we also reported transient neuronal swelling following SMF application (Fig. 8) which could be reversed by application of DIDS. These evidences support the involvement of SLC26A11 channels in Cl^- accumulation.

Our experiments using GlyH-101 as a potential blocker of SMF effects indicate that SMF action could be reversed by them. In addition, our voltage-clamp data indicates similarities in I–V characteristics with SLC26A11-mediated currents (Rungta et al., 2015). Considering these similarities, we propose

that SMF modulates these same channels. In addition to the already ascribed functions of these channels, we submit that they would act as a weak inhibitory shunt during normal neuronal activity mostly at depolarizing membrane potentials. However, on application of SMF, the basal conductance of these channels is enhanced (Fig. 10), enhancing the shunting effect at subthreshold membrane voltages reducing R_{In} and increasing rheobase currents. Furthermore, during sustained depolarization similar to periods of repetitive firing, the voltage-dependent strong currents produced after SMF application (Fig. 10) results in the reduction of the number of AP spikes fired (Fig. 9) producing an overall decrease in intrinsic excitability of neurons following SMF.

Delving deeper into the plausible mechanism of tSMS action on neurons, the neuronal membrane comprising the anisotropic lipid bilayer (Rosen, 2003b) interspersed with transmembrane proteins may undergo a plethora of changes in response to the SMF. An important clue to this effect is our observation that blockade of TTX-sensitive Na^+ channels during SMF application failed to depolarize the RMP, reduce R_{In}, and increase rheobase currents in our current-clamp recording using a high Cl^- internal solution. TTX binds deep into the pore of voltage-gated Na^+ channels in close proximity to the selectivity filter and exhibits use-dependent enhancement of block (Hille, 2001). In addition, binding of TTX impedes the return of voltage sensor in domain IV to resting conformation (Capes et al., 2012). This affects the
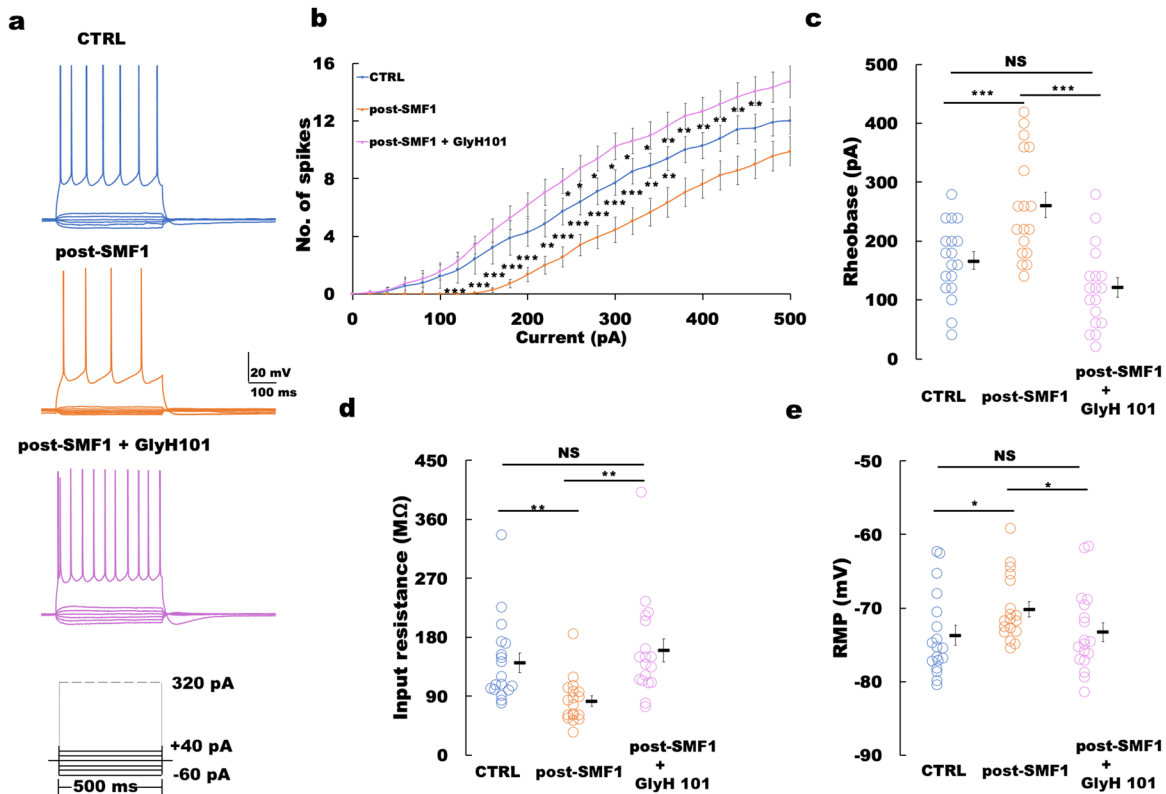
Figure 9. Reduced intrinsic excitability of layer II/III pyramidal neurons of the motor cortex following SMF application rescued by GlyH-101 block of Cl^- channels. ***a***, Representative subthreshold current injections (from −60 to +40 pA) with consequent voltage responses and repetitive firing by suprathreshold current injection (+320 pA) in the CTRL (blue), post-SMF 1 (orange), and post-SMF 1 + GlyH-101 (pink) groups. At the same subthreshold current injection, the voltage responses decreased in the post-SMF 1 group. At +320 pA current injection, the number of spikes for post-SMF 1 + GlyH-101 group exceed number of spikes elicited by CTRL group. Scale bar as shown in inset. ***b***, A significant decrease (K–W test; ***$p < 0.001$) in the I–O relationship for the post-SMF 1 (orange) group in comparison with both CTRL (blue) and post-SMF 1 + GlyH-101 (pink) groups. I–O relationship for post-SMF 1 + GlyH-101 significantly increased in comparison with CTRL group (K–W test; *$p < 0.05$; **$p < 0.01$). Error bars represent SEM. ***c–e***, Individual data points are shown as open circles in blue (CTRL, $n = 18$), orange (post-SMF 1, $n = 18$), and pink (post-SMF 1 + GlyH-101, $n = 18$). The mean values are indicated by solid bars next to the data points. Error bars represent SEM. Rheobase from layer II/III pyramidal neurons significantly increased in the post-SMF 1 group compared with CTRL and post-SMF 1 + GlyH-101 (one-way ANOVA; $p = 0.000004$; post hoc, Ryan–Einot–Gabriel–Welsch F test; post-SMF 1 vs post-SMF + GlyH-101 with ***$p < 0.001$; post-SMF 1 vs CTRL with ***$p < 0.001$) groups. No significant differences between post-SMF + GlyH-101 and CTRL groups (***c***). Input resistance of pyramidal neurons significantly lower in the post-SMF 1 group (K–W test; **$p < 0.01$; post hoc, stepwise step-down; post-SMF 1 vs post-SMF 1+ GlyH-101 with **$p < 0.01$; post-SMF 1 vs CTRL with **$p < 0.01$). No significant differences between post-SMF + GlyH-101 and CTRL groups (***d***). RMP of pyramidal neurons significantly lower in the post-SMF 1 group (K–W test; **$p < 0.01$; post hoc, stepwise step-down; post-SMF 1 vs post-SMF 1+ GlyH-101 with *$p < 0.05$; post-SMF 1 vs CTRL with *$p < 0.05$). No significant differences between post-SMF + GlyH-101 and CTRL groups (***e***).

electromechanical coupling between the inner gating pore and voltage sensor. A recent modelling study (Hernando et al., 2020) indicated that the application of SMF with inhomogeneous gradients induced surface tension along the neuronal membrane, effectively stretching them. They proposed that this mechanical force would be sufficient to interfere with the energy barriers governing the activation, inactivation, and deactivation of ion channels. Thus, we hypothesize that SMF action produces membrane deformation facilitating the movement of voltage sensor of Na^+ channels enhancing the Na^+ entry into the neurons. Thereafter, post-SMF the Cl^- entry through open Cl^- channels driven by the electrochemical driving force for Na^+ produce the prolonged shunting inhibition. As application of TTX blocks Na^+ entry and hinders transitions of the voltage sensor domain during SMF application, it prevents alteration in intrinsic excitability.

This study showed the neurophysiological mechanism of intrinsic plasticity in mice induced by moderate-intensity SMF with the same magnetic parameters as those of tSMS in humans. Intrinsic plasticity phenomenon is a nonsynaptic modulation of neuronal excitability (Titley et al., 2017; Debanne et al., 2019). Intrinsic plasticity has been reported to result from modifications of voltage- or calcium-dependent potassium channels (Schreurs

et al., 1998; Frick et al., 2004; Belmeguenai et al., 2010) as well as hyperpolarization-activated and cyclic nucleotide-gated (HCN) channels (Brager and Johnston, 2007). This is the first study to show that intrinsic plasticity may also be mediated by Cl^- channels. The relationship between intrinsic excitability changes and synaptic plasticity has been proposed to be synergistic (Debanne et al., 2019). This is important because in vitro correlates of learning paradigms (LTP/LTD) strictly adhere to protocols that essentially modify neuronal excitability. In addition, the observed temporary suppression of the intrinsic excitability of pyramidal neurons may lead to a consequential reduction in the excitatory synaptic output. However, considering that the dynamic phenomena of homeostatic synaptic scaling and Hebbian plasticity mechanisms are also at play, the intrinsic plasticity affected by the SMF action may impact neural coding. The enhanced shunting inhibition produced as a result of SMF (Figs. 2, 5, 9) may impact synaptic plasticity. Another interesting observation was that the SMF-induced GlyH-101-sensitive currents also showed a rapidly activating and inactivating current component during the step voltage protocol (Fig. 10a). This component of the Cl^- current would affect the summation of excitatory postsynaptic potentials (EPSPs). The regulation of $[Cl^-]_i$ in neurons is
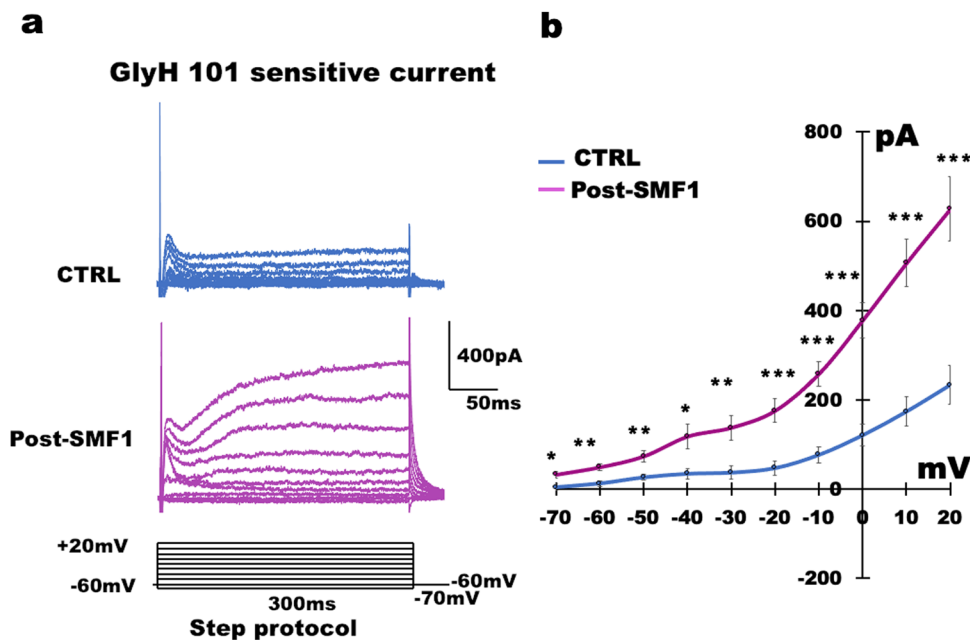
Figure 10. SMF application enhances GlyH-101-sensitive Cl⁻ currents with similar voltage dependence to SLC26A11. ***a***, Samples of GlyH-101-sensitive currents elicited by a voltage step protocol (from −70 to +20 mV; 300 ms) in the CTRL (blue) and post-SMF 1 + GlyH-101 (magenta) groups. ***b***, A significant enhancement of GlyH-101-sensitive currents (independent samples t test; **$p < 0.001$) as evidence by the current–voltage (I–V) relationship for the post-SMF 1 (magenta) group in comparison with CTRL (blue) group (CTRL, $n = 14$ cells; post-SMF 1, $n = 14$, 5 mice; t test, *$p < 0.05$; **$p < 0.01$; ***$p < 0.001$). Scale bar as shown in inset. Error bars represent SEM.

another fundamental factor for proper neural coding (Doyon et al., 2016) that affects GABA action and the subsequent summation of synaptic inputs. GABA decrease in the primary motor area (M1) was positively correlated with the degree of motor learning (Stagg et al., 2011), and GABA$_A$ receptor agonist depressed the use/practice-dependent plasticity of the M1 (Bütefisch et al., 2000; Ziemann et al., 2001). SMF action-mediated temporary changes in both intrinsic excitability and [Cl⁻]$_i$ would appear to affect learning. Indeed, it was reported that tSMS alters sequential implicit motor learning in humans (Nojima et al., 2019). This effect of tSMS on motor learning, in addition to our findings, would depend on the summation of network-level changes contributed by the SMF action on GABAergic interneurons, although the effect of SMF on motor learning remains to be investigated. Taken together, our findings suggest that tSMS can induce motor cortical plasticity in humans by regulating the activity of a certain type of Cl⁻ channel in neurons.

Data Availability

Data that support the findings will be made available upon reasonable request to the corresponding author.

References

Akita T, Okada Y (2014) Characteristics and roles of the volume-sensitive outwardly rectifying (VSOR) anion channel in the central nervous system. Neuroscience 275:211–231.

Alexander SP, Benson HE, Faccenda E, Pawson AJ, Sharman JL, Catterall WA, Spedding M, Peters JA, Harmar AJ, CGTP Collaborators (2013) The concise guide to pharmacology 2013/14: ion channels. Br J Pharmacol 170:1607–1651.

Beck H, Yaari Y (2008) Plasticity of intrinsic neuronal properties in CNS disorders. Nat Rev Neurosci 9:357–369.

Belmeguenai A, et al. (2010) Intrinsic plasticity complements long-term potentiation in parallel fiber input gain control in cerebellar Purkinje cells. J Neurosci 30:13630–13643.

Brager DH, Johnston D (2007) Plasticity of intrinsic excitability during long-term depression is mediated through mGluR-dependent changes in I(h) in hippocampal CA1 pyramidal neurons. J Neurosci 27:13926–13937.

Bütefisch CM, Davis BC, Wise SP, Sawaki L, Kopylev L, Classen J, Cohen LG (2000) Mechanisms of use-dependent plasticity in the human motor cortex. Proc Natl Acad Sci U S A 97:3661–3665.

Capes DL, Arcisio-Miranda M, Jarecki BW, French RJ, Chanda B (2012) Gating transitions in the selectivity filter region of a sodium channel are coupled to the domain IV voltage sensor. Proc Natl Acad Sci U S A 109:2648–2653.

Carrasco-López C, Soto-León V, Céspedes V, Profice P, Strange BA, Foffani G, Oliviero A (2017) Static magnetic field stimulation over parietal cortex enhances somatosensory detection in humans. J Neurosci 37:3840–3847.

Coots A, Shi R, Rosen AD (2004) Effect of a 0.5-T static magnetic field on conduction in guinea pig spinal cord. J Neurol Sci 222:55–57.

Daoudal G, Debanne D (2003) Long-term plasticity of intrinsic excitability: learning rules and mechanisms. Learn Mem 10:456–465.

Debanne D, Inglebert Y, Russier M (2019) Plasticity of intrinsic neuronal excitability. Curr Opin Neurobiol 54:73–82.

Di Lazzaro V, Musumeci G, Boscarino M, De Liso A, Motolese F, Di Pino G, Capone F, Ranieri F (2021) Transcranial static magnetic field stimulation can modify disease progression in amyotrophic lateral sclerosis. Brain Stimul 14:51–54.

Dileone M, Mordillo-Mateos L, Oliviero A, Foffani G (2018) Long-lasting effects of transcranial static magnetic field stimulation on motor cortex excitability. Brain Stimul 11:676–688.

Doyon N, Vinay L, Prescott SA, De Koninck Y (2016) Chloride regulation: a dynamic equilibrium crucial for synaptic inhibition. Neuron 89:1157–1172.

Duran C, Thompson CH, Xiao Q, Hartzell HC (2010) Chloride channels: often enigmatic, rarely predictable. Annu Rev Physiol 72:95–121.

Freitas C, Farzan F, Pascual-Leone A (2013) Assessing brain plasticity across the lifespan with transcranial magnetic stimulation: why, how, and what is the ultimate goal? Front Neurosci 7:42.

Frick A, Magee J, Johnston D (2004) LTP is accompanied by an enhanced local excitability of pyramidal neuron dendrites. Nat Neurosci 7:126–135.

Gonzalez-Rosa JJ, Soto-Leon V, Real P, Carrasco-Lopez C, Foffani G, Strange BA, Oliviero A (2015) Static magnetic field stimulation over the visual cortex increases alpha oscillations and slows visual search in humans. J Neurosci 35:9182–9193.

Hallett M (2000) Transcranial magnetic stimulation and the human brain. Nature 406:147–150.

Hernando A, Galvez F, García MA, Soto-León V, Alonso-Bonilla C, Aguilar J, Oliviero A (2020) Effects of moderate static magnetic field on neural systems is a non-invasive mechanical stimulation of the brain possible theoretically? Front Neurosci 14:419.

Hille B (2001) *Ion channels of excitable membranes*. Sunderland, MA, USA: Sinauer Associates, Inc. p. 534.

Hollis A, Zewdie E, Nettel-Aguirre A, Hilderley A, Kuo H-C, Carlson HL, Kirton A (2020) Transcranial static magnetic field stimulation of the motor cortex in children. Front Neurosci 14:464.

Hoogendam JM, Ramakers GMJ, Di Lazzaro V (2010) Physiology of repetitive transcranial magnetic stimulation of the human brain. Brain Stimul 3:95–118.

Inoue H, Mori S, Morishima S, Okada Y (2005) Volume-sensitive chloride channels in mouse cortical neurons: characterization and role in volume regulation. Eur J Neurosci 21:1648–1658.

Jang DC, Shim HG, Kim SJ (2020) Intrinsic plasticity of cerebellar Purkinje cells contributes to motor memory consolidation. J Neurosci 40:4145–4157.

Jentsch TJ, Pusch M (2018) CLC chloride 618 channels and transporters: structure, function, physiology, and disease. Physiol Rev 98:1493–1590.

Kirimoto H, Tamaki H, Matsumoto T, Sugawara K, Suzuki M, Oyama M, Onishi H (2014) Effect of transcranial static magnetic field stimulation over the sensorimotor cortex on somatosensory evoked potentials in humans. Brain Stimul 7:836–840.

Kirimoto H, Watanabe T, Kubo N, Date S, Sunagawa T, Mima T, Ogata K, Nakazono H, Tobimatsu S, Oliviero A (2020) Influence of static magnetic field stimulation on the accuracy of tachystoscopically presented line bisection. Brain Sci 10:1006.

Kobayashi M, Pascual-Leone A (2003) Transcranial magnetic stimulation in neurology. Lancet Neurol 2:145–156.

Kourrich S, Calu DJ, Bonci A (2015) Intrinsic plasticity: an emerging player in addiction. Nat Rev Neurosci 16:173–184.

Nojima I, Watanabe T, Gyoda T, Sugata H, Ikeda T, Mima T (2019) Transcranial static magnetic stimulation over the primary motor cortex alters sequential implicit motor learning. Neurosci Lett 696:33–37.

Oliviero A, Mordillo-Mateos L, Arias P, Panyavin I, Foffani G, Aguilar J (2011) Transcranial static magnetic field stimulation of the human motor cortex. J Physiol 589:4949–4958.

Paxinos G, Franklin KB (2019) *Paxinos and Franklin's the mouse brain in stereotaxic coordinates*. San Diego: Academic Press.

Rahmati N, Kunzelmann K, Xu J, Barone S, Sirianant L, De Zeeuw CI, Soleimani M (2013) Slc26a11 is prominently expressed in the brain and functions as a chloride channel: expression in Purkinje cells and stimulation of V H+-ATPase. Pflug Arch Eur J Physiol 465:1583–1597.

Rahmati N, Veloz MFV, Xu J, Barone S, Hamida NRB, Schonewille M, Hoebeek FE, Soleimani M, De Zeeuw CI (2016) SLC26A11 (KBAT) in Purkinje cells is critical for inhibitory transmission and contributes to locomotor coordination. Eneuro 3:1–16.

Rosen AD (1996) Inhibition of calcium channel activation in GH3 cells by static magnetic fields. Biochim Biophys Acta 1282:149–155.

Rosen AD (2003a) Effect of a 125 mT static magnetic field on the kinetics of voltage activated Na+ channels in GH3 cells. Bioelectromagnetics 24:517–523.

Rosen AD (2003b) Mechanism of action of moderate-intensity static magnetic fields on biological 654 systems. Cell Biochem Biophys 39:163–173.

Rungta RL, Choi HB, Tyson JR, Malik A, Dissing-Olesen L, Lin PJC, Cain SM, Cullis PR, Snutch TP, MacVicar BA (2015) The cellular mechanisms of neuronal swelling underlying cytotoxic edema. Cell 161:610–621.

Schreurs BG, Gusev PA, Tomsic D, Alkon DL, Shi T (1998) Intracellular correlates of acquisition and long-term memory of classical conditioning in Purkinje cell dendrites in slices of rabbit cerebellar lobule HVI. J Neurosci 18:5498–5507.

Shibata S, Watanabe T, Yukawa Y, Minakuchi M, Shimomura R, Ichimura S, Kirimoto H, Mima T (2021) Effects of transcranial static magnetic stimulation over the primary motor cortex on local and network spontaneous electroencephalogram oscillations. Sci Rep 11:8261.

Shibata S, Watanabe T, Yukawa Y, Minakuchi M, Shimomura R, Mima T (2020) Effect of transcranial static magnetic stimulation on intracortical excitability in the contralateral primary motor cortex. Neurosci Lett 723:134871.

Stagg CJ, Bachtiar V, Johansen-Berg H (2011) The role of GABA in human motor learning. Curr Biol 21:480–484.

Titley HK, Brunel N, Hansel C (2017) Toward a neurocentric view of learning. Neuron 95:19–32.

Tsuru D, Watanabe T, Chen X, Kubo N, Sunagawa T, Mima T, Kirimoto H (2020) The effects of transcranial static magnetic fields stimulation over the supplementary motor area on anticipatory postural adjustments. Neurosci Lett 723:134863.

Verkman AS, Galietta LJ (2009) Chloride channels as drug targets. Nat Rev Drug Discov 8:153–171.

Zhang W, Linden DJ (2003) The other side of the engram: experience-driven changes in neuronal intrinsic excitability. Nat Rev Neurosci 4:885–900.

Ziemann U, Muellbacher W, Hallett M, Cohen LG (2001) Modulation of practice-dependent plasticity in human motor cortex. Brain 124:1171–1181.